JGR Solid Earth

RESEARCH ARTICLE
10.1029/2022JB025316

Special Section:
Advances in understanding volcanic processes

Dynamics of Magma Chamber Replenishment Under Buoyancy and Pressure Forces

A. Longo[1], D. Garg[1], P. Papale[1], and C. P. Montagna[1]

[1]Istituto Nazionale di Geofisica e Vulcanologia, Sezione di Pisa, Pisa, Italy

Key Points:

- A numerical model for time-space dynamics in shallow magma chambers replenished by deep magma is presented
- Evolution under pressure and buoyancy forces is initially dominated by overpressure, and over the long term by buoyant convection and mixing
- Lifetime evolution of volcanic systems is likely toward stable conditions with no pressure buildup leading to an eruption

Supporting Information:

Supporting Information may be found in the online version of this article.

Correspondence to:

A. Longo,
antonella.longo@ingv.it

Citation:

Longo, A., Garg, D., Papale, P., & Montagna, C. P. (2023). Dynamics of magma chamber replenishment under buoyancy and pressure forces. *Journal of Geophysical Research: Solid Earth*, *128*, e2022JB025316. https://doi.org/10.1029/2022JB025316

Received 3 AUG 2022
Accepted 4 JAN 2023

Author Contributions:

Conceptualization: A. Longo, D. Garg, P. Papale
Data curation: A. Longo
Funding acquisition: P. Papale
Investigation: A. Longo
Methodology: A. Longo, D. Garg, P. Papale, C. P. Montagna

Abstract Active magma chambers are periodically replenished upon a combination of buoyancy and pressure forces driving upward motion of initially deep magma. Such periodic replenishments concur to determine the chemical evolution of shallow magmas, they are often associated to volcanic unrests, and they are nearly ubiquitously found to shortly precede a volcanic eruption. Here, we numerically simulate the dynamics of shallow magma chamber replenishment by systematically investigating the roles of buoyancy and pressure forces, from pure buoyancy to pure pressure conditions and across combinations of them. Our numerical results refer to volcanic systems that are not frequently erupting, for which magma at shallow level is isolated from the surface ("closed conduit" volcanoes). The results depict a variety of dynamic evolutions, with the pure buoyant end-member associated with effective convection and mixing and generation of no or negative overpressure in the shallow chamber, and the pure pressure end-member translating into effective shallow pressure increase without any dynamics of magma convection associated. Mixed conditions with variable extents of buoyancy and pressure forces illustrate dynamics initially dominated by overpressure, then, over the longer term, by buoyancy forces. Results globally suggest that many shallow magmatic systems may evolve during their lifetime under the control of buoyancy forces, likely triggered by shallow magma degassing. That naturally leads to long-term stable dynamic conditions characterized by periodic replenishments of shallow partially degassed, heavier magma by volatile-rich fresh deep magma, similar to those reconstructed from petrology of many shallow-emplaced magmatic bodies.

Plain Language Summary Periodic injections of magma into shallow magma chambers are a fundamental process known to govern the evolution of magmatic systems. According to our overall understanding of magmatic systems, we simulate the time-space dynamics in a composite magmatic system under the action of buoyancy and pressure forces. The formers are due to different chemical compositions of the shallow and deep magmas. The latter may result from chemical reactions, tectonic stress accumulation, or other deep processes. The numerical results illustrate an ample variety of situations mostly controlled by buoyancy or pressure forces. It is found that the "normal" condition for many volcanic systems is likely characterized by periodic arrivals of light batches of magma giving rise to efficient convection and mixing at shallow level, and parallel sinking of partially degassed, dense magma. This ensures essentially stable conditions unlikely to give origin to any pressure buildup leading to an eruption; it provides a mechanism for long life times of relatively small, shallow magmatic systems, and a framework for interpreting petrologic observations suggesting long sequences of mixing events at magmatic systems worldwide.

1. Introduction

Magmatic systems below active volcanoes can be extremely complex in terms of their shape, physical properties, and evolution (Annen et al., 2015; Burchardt et al., 2016; Cashman et al., 2017; Edmonds et al., 2019; Gudmundsson, 2020; Sparks & Cashman, 2017; Sparks et al., 2019, 2022; Tibaldi, 2015). Magmatic systems can extend vertically over several km, with the shallower portions located only a few km, sometimes <1 km, below the surface, connected through dyke systems to other reservoirs at different depths, and often to a larger one at depths approaching or exceeding 10 km (Cashman & Giordano, 2014). The shallow portion of such composite magmatic systems is typically more chemically evolved and partially degassed with respect to the deeper magma, as a result of interdependent processes such as cooling, crystallization, and degassing that are more efficient at shallow depth (Myers et al., 2014). Long lifetime to such shallow magmatic bodies, much in excess of estimated conductive cooling lifetimes, is provided by repeated magma injection events (Marsh, 2015) which add mass, heat, and volatiles, thus contrasting shallow-level cooling and degassing. Events of new injection at shallow level by deeper, chemically and physically distinct magma are often recognized to have shortly preceded the

Project Administration: P. Papale
Resources: P. Papale
Software: A. Longo, D. Garg
Supervision: P. Papale
Validation: A. Longo, D. Garg
Visualization: A. Longo, P. Papale
Writing – original draft: A. Longo, P. Papale
Writing – review & editing: A. Longo, D. Garg, P. Papale, C. P. Montagna

occurrence of a volcanic eruption (Colucci & Papale, 2021, and references therein). The dynamics associated with magma injection at shallow level are the subject of this work, specifically focusing on the roles of natural and forced convection, represented within magmatic systems by the buoyant and overpressurized systems addressed in this work, respectively. The different effects that pressure and buoyancy forces have on reservoir dynamics are investigated, as they are the main driving forces involved in magma transfer from deep to shallow crustal depths; their respective roles on magmatic interactions and eruption triggering are investigated.

The motion of a fluid, from single-phase single component (such as pure water) to multiphase multicomponent such as natural magma, relates to either natural or forced convection, or to a combination of them. Natural convection arises because fluids are immersed in the gravitational field, causing lighter portions to move up while denser portions sink down. The existence of density differences is therefore the cause of natural convection. In the case of real magmas, the melt phase of less chemically evolved (deeper) magmas tends to be denser than their evolved, shallow counterpart, as a reflection of larger content of heavy metals and lower content of light silicon more than compensating for higher temperature (Lange & Carmichael, 1990). Larger contents of heavy crystals such as olivine and pyroxene add to the density excess by more mafic magmas. However, shallow magmas get degassed as a reflection of the largely dominant role of pressure on volatile saturation, as can be inferred from measuring gas emissions at quiescent volcanoes or fumaroles (Aiuppa et al., 2019; Burgisser & Degruyter, 2015; Edmonds et al., 2022). At shallow crustal depths, magmas tend to stall and evolve in composition toward more felsic, water-richer, less dense melt phases than basaltic magmas. At those depths, though, exsolved magmatic fluids tend to decouple from the multiphase magmatic mixture as bubbles grow in size with decreasing pressures, favoring net loss of volatile phases. On the contrary, in more primitive magmas ascending from depth, the exsolved volatile phase consists of smaller bubbles that remain trapped into the melt contributing to overall multiphase density decrease (Gonnermann & Manga, 2007; Myers et al., 2014). In particular, the largely insoluble carbon dioxide component is quickly lost at shallow depth. Because the presence of carbon dioxide causes more water exsolution and the generation of a larger volume of gas at equal other conditions (Papale et al., 2022), and because of the order of magnitude difference, increasing with decreasing pressure thus depth, between the density of the melt + crystals and gas phases, it follows that magmas coming from depth can be lighter than the more evolved, partially degassed magmas they encounter at shallower depth, giving rise to natural convection.

Natural convection in magmas has been investigated mostly focusing on either thermal or compositional diffusion, that in turn modify the density of the magmatic multiphase mixture (Campbell, 1996; Clark et al., 1987; Oldenburg et al., 1989; Spera et al., 1982) causing denser components to sink. Diffusive processes in magma typically happen on much longer time scales than buoyancy-dominated interactions, as the Rayleigh number, indicating the ratio between time scale of buoyancy due to density differences and the smoothing effect on density differences due to diffusivity, is large (e.g., Bartlett, 1969).

In contrast with natural convection, forced convection relates to fluid motion governed by forces different from buoyancy. An example of forced convection is fluid motion inside a blender, or the motion of air in a room when a hair dryer is turned on (more precisely, the latter is a combination of natural and forced convection as the density of the air exiting the hair dryer is normally lower than ambient density). In magmatic environments, forced convection can arise as a consequence of chemical processes causing phase changes within confined systems leading to pressure increase, stress accumulation by local or regional tectonics, or by mantle or subduction dynamics. In all cases, forced convection requires the buildup of exceeding pressure somewhere in the system.

Magma motion is invariably associated with either a density difference, or some other force resulting in a pressure difference. Accordingly, deep magma can intrude a shallow reservoir either because it is lighter than the magma hosted in the reservoir (buoyancy force), or because it is pushed from below (pressure force), or because of a combination of both. Here, we examine the entire spectrum from pure buoyancy (Papale et al., 2017) to pure pressure triggering magma injection, through variable combinations of buoyancy and pressure. We describe markedly different system evolutions under the analyzed conditions, and show that while efficient convection and mixing require buoyancy, the conditions for rock fracturing, dyke propagation, and occurrence of a new eruption are unlikely to be met if pressure forces are not involved. We suggest that shallow magma chambers at closed conduit volcanoes evolve under essentially pure buoyant conditions over a substantial part of their lifetime, while the generation of a new eruption is associated with sufficient pressure buildup somewhere in the magmatic system.

In this work, we show results from numerical simulations of shallow magma reservoir replenishment focusing on the specific case of Campi Flegrei, in southern Italy, one of the highest volcanic risk areas in the world (Orsi

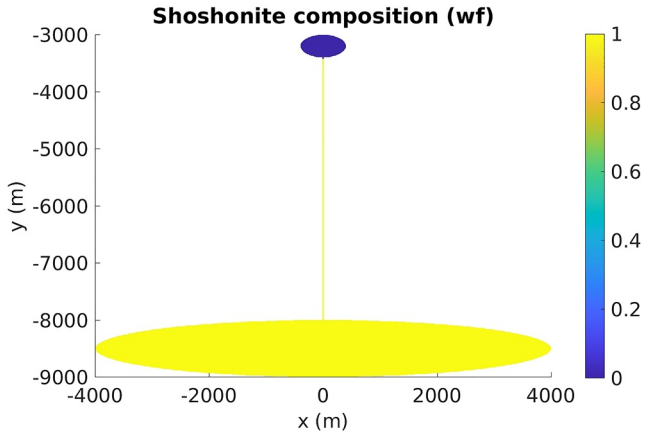

Figure 1. System setup. Colorbar reports magma composition weight fraction: 0 corresponds to phonolite, 1 corresponds to shoshonite. The system is simplified as being 2D (Cartesian). A shallow elliptical 800 × 400 m reservoir hosting phonolitic magma is connected through a vertical dyke with constant width of 20 m to a deeper and larger (8 × 1 km) reservoir hosting shoshonitic magma. A flat magma interface is placed at shallow chamber entrance. Buoyancy at magma interface is varied by assuming different volatile contents (water and carbon dioxide) in the two magma types. When applied, an initial homogeneous surplus in pressure is imposed to the shoshonitic magma, beyond the initial magmastatic stratification in pressure. The conditions for the executed numerical simulations are reported in Table 1.

et al., 2022). Geophysical (De Siena et al., 2010; Judenherc & Zollo, 2004; Zollo et al., 2008) and geochemical (Arienzo et al., 2009; Di Renzo et al., 2011) evidence suggests that the plumbing system at Campi Flegrei consists of a large, deep reservoir hosting shoshonitic magmas (Mangiacapra et al., 2008), and shallower reservoirs that host slightly more evolved phonolitic magmas (Arienzo et al., 2010). Pre-eruptive arrival of volatile-rich more primitive magmas into these shallower reservoirs has been often observed in the petrologic record at Campi Flegrei (Tonarini et al., 2009).

2. Methods

2.1. The Setup

Figure 1 shows the setup for the simulations. The system geometry is constructed in order to be the simplest one holding the fundamental aspects relevant to the analysis. The 2D simulation setup reduces computational costs without losing the fundamental details on the dynamics within the magmatic system (Garg et al., 2019). The setup includes a large, 8-km deep reservoir hosting shoshonitic magma, connected through a vertical dyke to a shallow, 3-km deep, much smaller reservoir hosting more evolved phonolitic magma (Table 1). The compositions employed for the shoshonitic and phonolitic magmas are reported in Table 2. The two end-member compositions are very similar, and have been chosen as representative of magmas erupted at Campi Flegrei that show evidence of pre-eruptive mingling and mixing (Arienzo et al., 2011). Volatile contents (water and carbon dioxide) are varied within reasonable ranges in order to simulate conditions with variable buoyancy. The volatile content of the deep shoshonite is taken as being the same for all simulations, and variable conditions are obtained by varying, from one simulation to the other, the volatile content of the shallow phonolite (Table 1). In all simulations, the deeper shoshonitic magma is assumed to carry a total (dissolved plus exsolved) volatile content corresponding to 2 wt% total water and 1 wt% total carbon dioxide. There is uncertainty on the total volatile contents for Campi Flegrei magmas, as for many other volcanoes, because it is a difficult data set to obtain from erupted products (e.g., Métrich et al., 2010). The ensemble of data on melt inclusions at Campi Flegrei (Arienzo et al., 2009; Mangiacapra et al., 2008), together with the application of a quantitative method to retrieve total volatile contents from the dissolved ones (Papale, 2005) and with the very high measured carbon

Table 1
Simulations Performed

Simulation name	H_2O^T (wt%)[a]	CO_2^T (wt%)[a]	$\Delta\rho$ (kg/m^3)[b]	ΔP (MPa)	Ar[c]	Hg[d]	Hg/Ar	Simulation time (s)
P0	1	0.1	162.45	0	0.60×10^9	0	0	4,870
P5	1	0.1	144.50	5	0.69×10^9	0.25×10^{13}	0.35×10^4	7,030
P3.5	1	0.5	92.27	3.5	0.39×10^9	0.15×10^{13}	0.39×10^4	5,340
P6.5	0.77	1	32.05	6.5	0.06×10^9	0.13×10^{13}	2.07×10^4	5,770
N5	2	1	−60.99	5	0	0.90×10^{13}	–	1,570
N10	2	1	−78.39	10	0	1.80×10^{13}	–	1,630
N15	2	1	−93.85	15	0	2.84×10^{13}	–	1,670

[a]Volatile contents refer to the phonolitic magma, whereas for the initially deeper shoshonitic magma these values are H_2O^T = 2 wt% and CO_2^T = 1 wt% for all simulations. [b]$\Delta\rho$ corresponds to the density difference between the shallow phonolite and the deep shoshonite, computed at the initial interface. [c]Archimedes number expressing buoyancy over friction force: $Ar = \rho\Delta\rho g L^3/\mu^2$. Ar = 0 when $\Delta\rho < 0$. L is the characteristic length of the system equals the width of the shallow chamber (800 m). Magma viscosity μ corresponds to the average viscosity value between the shallow phonolite and the deep shoshonite, computed at the initial interface. [d]Hagen number expressing pressure over friction force: $Hg = \rho\Delta P L^3/L_z\mu^2$. L_z is the characteristic length over which the pressure drop takes place; It corresponds to the height of the shoshonite-phonolite interface and is taken as 1 m.

Table 2
Volatile-Free Melt Composition Employed in the Simulations

	SiO_2	TiO_2	Al_2O_3	Fe_2O_3	FeO	MnO	MgO	CaO	Na_2O	K_2O
Phonolite	53.52	0.60	19.84	1.60	3.20	0.14	1.76	6.76	4.66	7.91
Shoshonite	52.40	0.85	17.60	1.88	5.74	0.12	3.60	7.93	3.43	8.24

Note. Quantities in wt%.

dioxide flux at Solfatara of Campi Flegrei (Chiodini et al., 2015) suggest that a few percent by weight for total carbon dioxide is a reasonable value.

The dyke is assumed to initially host the deeper shoshonitic magma, therefore, time zero for all simulations refer to an idealized moment when the deep ascending magma encounters the shallow reservoir. For the simulations with an initial overpressure, that overpressure is applied to the shoshonitic magma at time 0, as if the dyke was reaching the shallow chamber and rupturing the last diaphragm separating the dyke from the chamber. The applied initial overpressure is imposed as a constant surplus with respect to the local, stratified pressure distribution reflecting the nonlinear interplay between density, dissolved and exsolved volatile contents, and pressure. The Supporting Information S1 reports the initial vertical profiles of relevant quantities.

While the overall system in Figure 1 is closed, the results illustrated below can be seen as describing the open system evolution of the shallow chamber. Accounting for the large system in Figure 1 ensures global consistency of the dynamics in terms of evolution of the conditions characterizing the magma that is injected into the chamber. That leads to the rich dynamics illustrated in this work, and to results that describe in a globally consistent way the evolution over a large magmatic system including the large, deeper regions of magma accumulation. The complex evolutions described below would hardly be revealed had we aimed at describing magma chamber replenishment without accounting for the interconnections with deeper subdomains, represented here by a large, deep, less chemically evolved, less degassed magmatic reservoir, and the dyke connecting the deep and shallow reservoirs.

Table 1 illustrates the conditions for the numerical simulations. The two critical parameters for this study are the initial overpressure applied to the shoshonitic magma, and the density difference at the initial magma interface. For the three cases with no initial buoyancy (simulation names starting with "N" in Table 1), the total volatile contents in the two magma types are equal. Therefore, in these cases, the gas volume fraction and density differences at interface reflect the slightly different saturation conditions due to different melt composition, and the overpressure applied to the shoshonitic magma. In the cases with buoyancy (simulation names starting with "P") the upper phonolitic magma is assumed to host a lower total volatile content with respect to the shoshonitic magma (Table 1), as it may result from shallow system degassing. The assumed total volatile content in the phonolite, the different overpressure applied in the shoshonite, and the corresponding density modeling and saturation conditions, determine the density of the two magma types, therefore the magnitude of the initial buoyancy force acting at the interface.

2.2. Numerical Model

The dynamics of magma chamber replenishment for the setup described above is investigated with a model that treats magma as a multiphase, multicomponent fluid mixture, solving the compressible Navier-Stokes equations (details are in the Supporting Information S1; Garg et al., 2018a).

Partition between the liquid and gas phases is computed with the nonideal multicomponent saturation model SOLWCAD (Papale et al., 2006) as a function of space and time and depends on local composition, pressure, and temperature. Density and viscosity are calculated accordingly (Longo, Barsanti, et al., 2012; Montagna et al., 2015, 2022; Papale et al., 2017). The SOLWCAD model allows to realistically reproduce volatile saturation, including the reciprocal effect of different volatile species (H_2O and CO_2) in affecting their dissolved amounts. The accurate computation of gas exsolution is a priority since it has a major effect on magma properties (i.e., density and viscosity) that in turn strongly control magma fluid dynamics.

The Navier-Stokes equations are solved with the in-house finite element code GALES (Garg et al., 2018a; Longo, Barsanti, et al., 2012, Longo, Papale, et al., 2012; Papale et al., 2017). To keep the computational efforts to within

manageable size, the temperature is taken constant (1300 K) throughout the computational domain, and crystallization is neglected.

The code has been recently further developed to improve numerical stability (Garg et al., 2018a), include free surface dynamics (Garg et al., 2018b), fluid-structure interaction dynamics (Garg et al., 2021), and fully 3D dynamics (Garg & Papale, 2022). The reader interested in further details of the mathematics, the numerical methods, and the code stability and performance is addressed to such papers.

Employing a large system, such the simulated one, to reproduce the injection dynamics has a cost in terms of required computational resources. A resolution of 1 m is needed in the shallow chamber and dyke, where the dynamics is fast and the spatial dimensions, especially the dyke width, are small; while a resolution of 8 m is enough for the deep chamber where nearly no dynamics takes place.

3. Results and Discussion

The simulation results show totally different dynamic situations for the cases where buoyancy is effective ("P" simulations in Table 1) or is absent ("N" simulations). In the following we describe the buoyant cases first, then we consider the not buoyant cases. The focus is initially on the dynamics of shallow chamber replenishment and the relative roles of buoyancy and pressure forces in controlling those dynamics. The overall dynamics down to the deep chamber are described later.

To assess the relative importance of buoyancy and pressure forces, two nondimensional numbers are employed (see Table 1): Ar or the Archimedes number, representing the ratio between buoyancy and viscous forces; and Hg or the Hagen number, representing the ratio between pressure and viscous forces. The Hg/Ar ratio indicates therefore the relative roles of pressure and buoyancy forces.

The Archimedes and Hagen numbers can be derived from the adimentionalization of the momentum conservation equation for a fluid with pressure and density variations

$$\rho\frac{\delta v}{\delta t} + \rho(v\cdot\nabla)v = -\nabla p + \mu\nabla^2 v - g\Delta\rho$$

where v is velocity, t is time, p is pressure, ρ is density. On the left-hand side of the equation, the pressure, viscous, and buoyancy terms determine the space-time variations of velocity. Viscosity is opposed to both pressure and buoyancy forces. Therefore, the characteristics velocities of pressure forces and buoyancy forces are derived by equating the pressure and buoyancy terms to the viscous term. It results that $v_{buoyancy} = \frac{g\Delta\rho L^2}{\mu}$ and $v_{pressure} = \frac{\Delta p}{L_z}\frac{L^2}{\mu}$, where $\Delta\rho$ and Δp are the steps in density and pressure at the shoshonite-phonolite interface, and L_z the width of the interface. The two characteristic velocities are inserted into the Reynolds number to state the corresponding flow regime. After substitution, the Archimedes and Hagen numbers are obtained

$$Ar = \frac{g\rho\Delta\rho L^3}{\mu^2}$$

$$Hg = \frac{\Delta p\rho L^3}{L_z\mu^2}$$

3.1. Buoyant Systems

In buoyant systems the shallow chamber contains degassed heavier magma, while the deep chamber and conduit are filled with volatile-rich lighter magma. In the pure-buoyancy case P0 (see Table 1) the pressure vertical profile is magmastatic. In cases P5, P3.5, and P6.5 (see Table 1) the lower part of the system is overpressurized. Simulation P0 is similar to the pure buoyant end-member case explored in Papale et al. (2017). Here, we briefly summarize the main characteristics of the dynamics, which are fully described in the above paper; and employ them as a reference to compare with the other cases involving both buoyancy and pressure. In general, we present the four "P" simulations in order of increasing Hg/Ar ratio (Table 1), which corresponds to progressively decreasing buoyancy (but not progressively increasing pressure). The Supporting Information S1 includes videos showing the space-time evolution of composition for all simulations in Table 1.

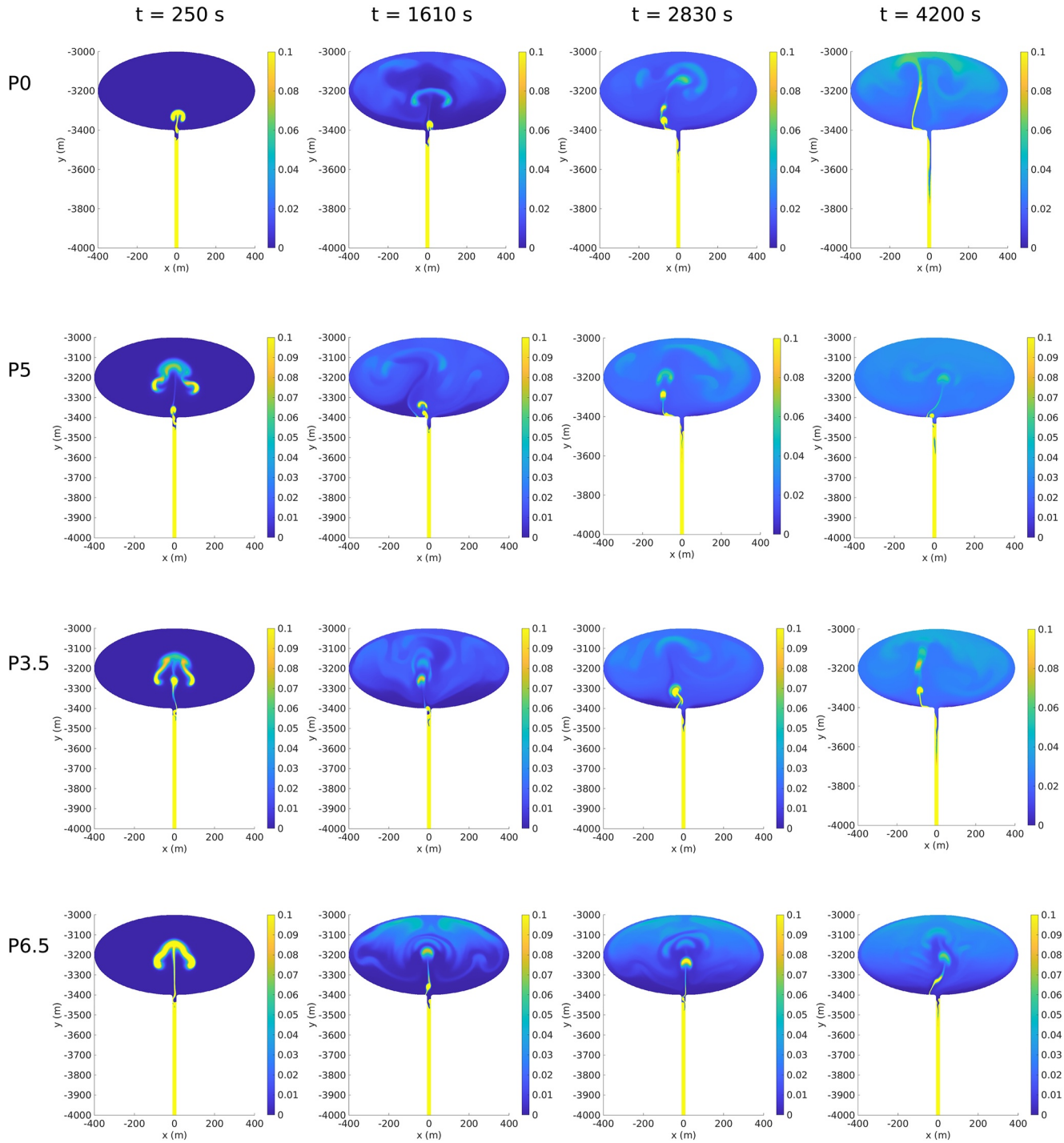

Figure 2. Computed evolution of composition for the buoyant simulation cases. The figures show a zoom view of the shallow chamber and upper portion of the feeding dyke.

When convective motion is triggered by pure buoyancy (case P0), the numerical simulation results show quick disruption of the initial gravitationally unstable interface followed by formation and ascent of intermittent plumes of light magma. Such plumes penetrate into the shallow chamber forming complex circulation patterns which enhance mixing between the two magmas (Figure 2; note that at the resolution of the present simulations, of order 1 m, only mechanical mixing, sometimes referred to as "mingling," is resolved; Petrelli et al., 2011). The system we model is closed, therefore injection of light magma into the chamber is accompanied by sinking of the initially resident, partially degassed, denser magma into the dyke, resulting in net mass loss from the

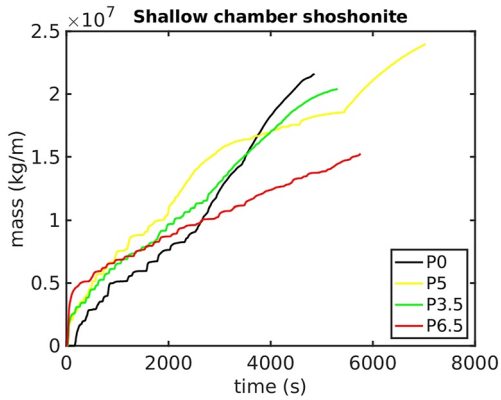

Figure 3. Time evolution of the mass of shoshonite in the shallow chamber, for the four buoyant simulation cases. Mass of shoshonite is computed as the integral of the quantity $\alpha_{shoshonite}\rho_{shoshonite}$ over the whole shallow chamber area. $\alpha_{shoshonite}$ is the volume fraction of shoshonite and $\rho_{shoshonite}$ is the density of shoshonite.

shallow reservoir (Papale et al., 2017). Mixing between the two magmas is mostly effective at dyke level, such that immediately after the very first initial plume no further pure shoshonite enters the chamber. Correspondingly, the new plumes after only a few minutes contain at most 50% by weight of the deeper shoshonitic component. Efficient mingling within feeding conduits and dykes has been postulated by recent conduit flow models, enhanced by the presence of bubbles (Wei et al., 2021). The dynamics evolve through a series of discrete plumes of variable size releasing buoyant mixed magma into the chamber, further accompanied by sinking of denser magma into the dyke. A dynamic stratification of composition and properties is built inside the chamber. The overall stratification is continuously disrupted to an extent by new buoyant plumes, then rebuilt until the next plume disrupts it again. The successive light plumes accumulating downwards from the top of the denser reservoir progressively decrease the density of the shallow chamber inhibiting the efficiency of mass exchange. The observed mingling dynamics is, albeit on much larger spatial scales, in good agreement with the experimental results obtained on similar systems (Montagna et al., 2015; Morgavi et al., 2013a, 2013b; Perugini et al., 2015), providing good confidence in their validity. For the pure buoyant case, the longer simulations in Papale et al. (2017) show waning of the dynamics for times greater than 4–7 hr depending on the specific simulation conditions. Beyond those times a condition of dynamic equilibrium is achieved, in which slow dynamics are still ongoing but all macroscopic quantities in the shallow chamber (e.g., the overall mass of components) do not significantly evolve anymore.

When an initial overpressure is added to the rising magma (cases P5, P3.5, and P6.5 in Table 1 and Figure 2), the overall dynamics are qualitatively similar to those described above, dominated by discrete plumes accompanying the overall injection-sinking dynamics. There are, however, important quantitative differences, and most importantly, there are substantial differences in relation to the distribution and evolution of overpressure.

After 250 s from simulation start (Figure 2), there is a well visible plume rising in the shallow chamber in all simulation cases. However, at that time, the plume reaches a height in the chamber of only about 100 m for the pure buoyant case P0, whereas that height at the same time is 270–290 m for the three cases with nonzero overpressure. Thus, the existence of an initial overpressure in the injected magma is seen as a clear push during the first few minutes of interaction. For the two intermediate cases with applied overpressure of 3.5 and 5 MPa, the initial batch of rising magma appears to be formed by at least two individual plumes shortly following one another, while for the case with highest overpressure of 6.5 MPa, the initial rising batch appears as a well-identified individual plume.

Figure 3 shows the evolution in time of the mass of intruding shoshonite in the shallow chamber. The time series illustrate the interplay between buoyancy and overpressure in driving the overall dynamics. The increase in overpressure appears to exert an important control on the initial dynamics, as it is exemplified by a stronger push of light magma into the chamber and initially faster rising plume and sinking front: the applied overpressure triggers a more rapid development of the Rayleigh-Taylor gravitational instability (Chandrasekhar, 1961). However, the long-term overall dynamics appears to be more directly driven by buoyancy, which exerts a strong control on mixing efficiency (Montagna et al., 2015). The curves in Figure 3 show an initial phase where pressure dominates in forcing the shoshonite into the chamber, followed by a longer phase where buoyancy takes the lead and finally determines the overall efficiency of magma injection. The trends in Figure 2 show a crossover with respect to the pure buoyancy case, which happens sooner for less buoyant conditions. Over the long term, the least effective case in injecting new magma into the shallow chamber is the one (P6.5) associated with the largest overpressure but lowest buoyancy conditions (i.e., reflected in far less effective mixing for case P6.5 well visible from Figure 2 as a dark blue color over much of the shallow chamber at the longest reported time). That same case was instead the most effective during the initial stages, reflecting the large push by overpressure. After the initial overpressure-dominated transient, the most effective case (P0) is the one with highest buoyancy and lowest (zero) overpressure, which was initially associated to a much less effective injection dynamics (Figures 2 and 3). Convective efficiency, associated with mass exchange among the two magmatic components in the shallow reservoir, has been observed to follow and exponentially decreasing trend in time (Montagna & Papale, 2018; Morgavi

et al., 2013a, 2013b). Therefore, the mingling process will slow down until it asymptotically reaches equilibrium (Papale et al., 2017). Simulations are stopped as the initial pressure-driven transient is over, and buoyant convection becomes dominant.

To interpret these results, pressure-driven and buoyancy-driven replenishment time scales can be estimated to first order from first principles. The pressurized, deep part of the domain relaxes on time scales dictated by the speed of sound in the system. To first approximation, the latter can be estimated from density ρ and compressibility β as $c^2 = 1/\rho\beta$. Constitutive equations employed here yield values of $\rho \sim 2{,}500$ kg/m^3 and $\beta \sim 10^{-9}$ Pa^{-1} (Longo, Barsanti, et al., 2012), thus we can estimate $c \sim 600$ m/s. Given the size of the simulated system, see Figure 1, pressure disturbances are expected to propagate through the system on time scales of tens of seconds. Unless we deal with much shallower magmatic systems, where volatile exsolution has a much larger impact on compressibility, similar numbers are valid for the majority of volcanic plumbing systems at crustal depths. Time scales for the Rayleigh-Taylor gravitational instability are known in the linear regime only (Bellman & Pennington, 1954), therefore for the initial destabilizing phases; nevertheless, the parameters that impact on the rise (and sink) velocities remain the same for the whole dynamical evolution. Rayleigh-Taylor growth rate γ for the most instable wavelength can be expressed as (Menikoff et al., 1977)

$$\gamma = \frac{g^{2/3}}{2}\sqrt[3]{\frac{\mathrm{A}^2}{\hat{\nu}}},$$

where g is gravitational acceleration; $\mathrm{A} = (\rho_2 - \rho_1)/(\rho_2 + \rho_1)$ is the Atwood number; and $\hat{\nu} = (\mu_1 + \mu_2)/(\rho_1 + \rho_2)$ is the density-weighted average viscosity. Available wavelengths are limited by the intruding dyke width; nevertheless, the dependency on the physical properties of magmas remains the same.

The most important factor in determining the growth rate is the density contrast, expressed by the Atwood number, which is typically very small for magmatic systems. Higher viscosities tend to hamper the development of the instability. A characteristic time scale can be expressed as the inverse of the growth rate. For our simulations, $A \sim 10^{-1}$ and $\hat{\nu} \sim 10^{-1}$, yielding typical time scales on the order of seconds. While the Atwood number is not expected to vary much for any magmatic systems, magmatic viscosities can vary widely, therefore much longer time scales are expected for the development of gravitational instabilities in more viscous, evolved magmas. The long-term mixing efficiency thus increases with $\Delta\rho$ and decreases with viscosity (Montagna et al., 2015). In other words, it decreases with Archimedes number Ar from P0, to P5, to P3.5, and P6.5 as illustrated in Figure 3 (line corresponding to simulation P3.5 intersects and falls below line corresponding to case P5 over times longer than those simulated).

The above results are illustrative of the relative roles of buoyancy and overpressure in the efficiency of new magma injection into a shallow chamber. In extreme synthesis, while overpressure dominates initially, the overall process is mostly controlled by buoyancy. However, in terms of likelihood of causing rock fracturing, new dyke injection, and eruption, the existence of an overpressure in the ascending magma is key.

Figure 4 shows the evolution of overpressure (defined as the locally computed difference between pressure at current and zero time) in the shallow chamber for the four buoyant simulation cases. Figure 5 illustrates the time evolution of the average shallow chamber overpressure, obtained by weighting the overpressure at any computational node by its corresponding area. The figures highlight macroscopic differences associated with the different conditions in the simulations. The most relevant of such differences is that the sign of the pressure change is negative for the pure buoyant case (P0), and positive for all other cases involving an initially applied overpressure. Counter-intuitive pressure decrease upon chamber replenishment driven by pure buoyancy force is discussed in detail in Papale et al. (2017). In summary, pressure evolution is nonlinearly correlated to density and gas volume fraction. While expansion upon gas exsolution exerts a force on the surroundings which contributes to increasing pressure, substitution of dense magma by lighter one implies a net decrease of mass in the chamber and a decrease in the magmastatic pressure contribution, favoring decreasing pressure. For the conditions investigated in Papale et al. (2017) and here, pure buoyancy-driven magma injection at shallow level results in either very small (or negligible) increase or significant decrease in overall pressure, with the magnitude of the pressure change increasing with increasing initial density difference (thus with increasing Ar in Table 1). Figure 5 shows that for case P0 at the longest simulated time approaching 5,000 s, the average chamber pressure decreases by about 0.55 MPa. Because of the magmastatic contribution to pressure decrease, the magnitude of the decrease increases with depth inside the chamber (Figure 4, case P0).

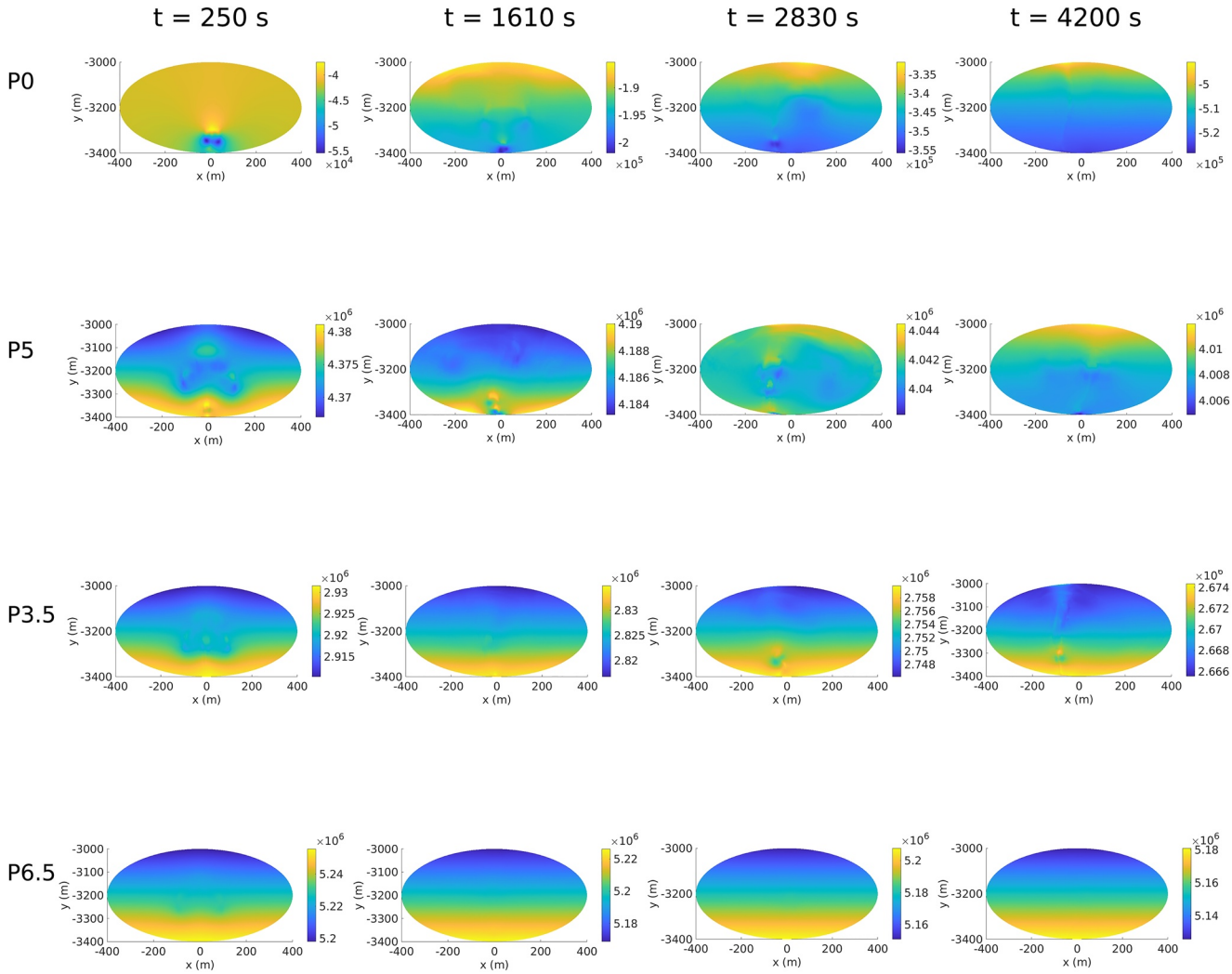

Figure 4. Evolution of overpressure in the shallow magma chamber for the simulation cases with nonzero buoyancy.

For the three cases with associated overpressure, the pressure change is always positive during the entire simulated times (Figures 4 and 5), although appreciably lower than the applied overpressure. The peak overpressure in the chamber is achieved over a short time scale in the range 10–100 s. After that initial pulse, the average chamber overpressure slightly and progressively decreases (Figure 5). The extent to which the applied overpressure is

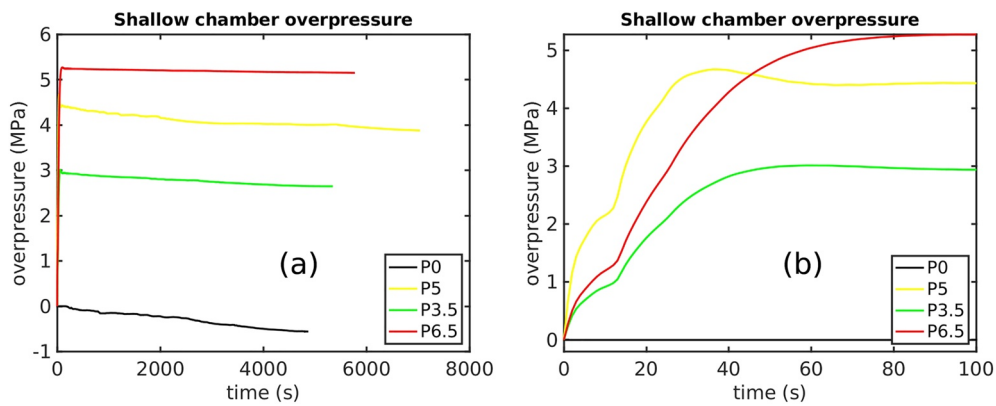

Figure 5. Evolution of the average overpressure in the shallow chamber, for the simulation cases with nonzero buoyancy (cases "P" in Table 1). (a) Evolution over all simulated times. (b) Zoom over the first 100 s.

transferred into the chamber depends on a number of factors, including magma compressibility which varies from case to case. In the present cases, the maximum average overpressure in the chamber is in the range 80%–90% of the applied one. Over the times displaced in Figure 5, the maximum overpressure decreases after the initial pressure pulse amounts to 4%–14% (about 0.2–0.4 MPa) of the achieved peak value. The extent of shallow chamber pressurization in cases P3.5, P5, and P6.5 is in the interval 3–5 MPa. According to Gudmundsson (2012), an excess pressure similar to the in situ tensile strength of the host rock, 0.5–9 MPa, is required to open a conduit toward the surface. An overpressurization such as that considered in this work is needed to trigger an eruption.

The above trends depict an initial phase, with time length of order 1 min, dominated by overpressure, followed by a much longer phase of order hours where buoyancy governs the dynamics causing progressive although limited decrease in overpressure. The applied overpressure is only marginally (10%–20% for the range of conditions examined here) absorbed by magma compressibility and/or dissipated by internal friction, and largely transferred into the chamber. The longer buoyancy-dominated phase, in all four simulation cases with buoyancy, accounts for chamber pressure decrease by only one-tenth of MPa, progressively decreasing in magnitude (for the longest simulated times) from 0.55 MPa for case P0 with no applied overpressure, to 0.21 MPa for case P6.5 with the largest applied overpressure of 6.5 MPa. With reference to the two cases P3.5 and P6.5 where an initial overpressure is associated with least buoyant conditions, during the entire simulation time the overpressure in the chamber decreases from bottom to top (Figure 4). That situation is opposite to that of the pure buoyant case P0, where the overpressure increases (it becomes less negative) from bottom to top. The evolution of case P5, which involves both significant overpressure and buoyancy, is peculiar. For this case the evolution during the first about 2,000 s is similar to that of the two other cases with overpressure. However, shortly after 2,000 s a sort of overturning of the overpressure occurs, causing the distribution of overpressure to become, from there on, similar to that of the pure buoyancy case P0 (overpressure increasing upwards). Once again, the interplay of buoyancy and pressure forces in controlling the dynamics emerges, with the latter causing a downward increase in overpressure, and the former an upward increase (or in other words, both causing a downward increase in the magnitude of the overpressure, with positive sign for pressure force, and negative sign for buoyancy force). Pressure controls the processes initially, then buoyancy becomes dominant. If pressure forces are large enough with respect to buoyancy forces, the downward-increasing pressure-controlled stratification of overpressure is sufficiently stable and it does not get disrupted by subsequent buoyancy control of the dynamics. If instead the relevance of buoyancy increases with respect to the pressure force, then the initially pressure-controlled stratification in overpressure can lead the way to subsequent control by buoyancy, as in the present case P5. Comparison between the cases P5 and P3.5 suggests that such an overturning in the stratification of overpressure may appear for Be/Ar less than about 3.5 (Table 1).

3.2. Nonbuoyant Systems

The simulation cases N5, N10, and N15 in Table 1 do not involve any gravitational instability, as the initial distribution is such that magma density increases everywhere along the direction of gravity. In these cases, the dynamics are entirely due to pressure forces, which are applied in the form of an initial overpressure in the initially deeper shoshonitic magma, by 5, 10, and 15 MPa for the three cases above, respectively. Figure 6 (analogous to Figure 2) illustrates the numerical results in terms of distribution of composition. When buoyancy is not acting on the system, the dynamics are very limited. In all three simulated cases, there is an initial phase (order a few tens of s) of expansion of the compressed shoshonite into the phonolite, which is in turn compressed, followed by lateral flow of the dense shoshonite over the chamber bottom. Despite shoshonite is decompressed, volatile exsolution is not enough for it to become lighter than the overlying phonolite, so that no gravitational instability occurs at the interface. The entire dynamics are practically over after a few hundred seconds. After 1,000 s no further changes are visible. Mixing is limited to a thin region at the interface between the two magma types. Essentially, the dynamics consist in limited magma intrusion at chamber bottom accompanied by compression taking 70–100 s to achieve a new stable pressure profile in the chamber (Figure 7). As for the buoyant cases seen above, part of the initial overpressure is accommodated by magma compressibility. The proportion of the initially applied overpressure translating into stable chamber overpressure is close to 80% in all three cases (the volatile contents, thus the overall magma compressibility, are also the same for these three simulation cases, see Table 1).

The total mass of shoshonite which is displaced into the chamber (more precisely, displaced above the initial interface) is significantly lower than for the cases with buoyancy, amounting to 3.2, 6.2, and 9 Mkg/m for the

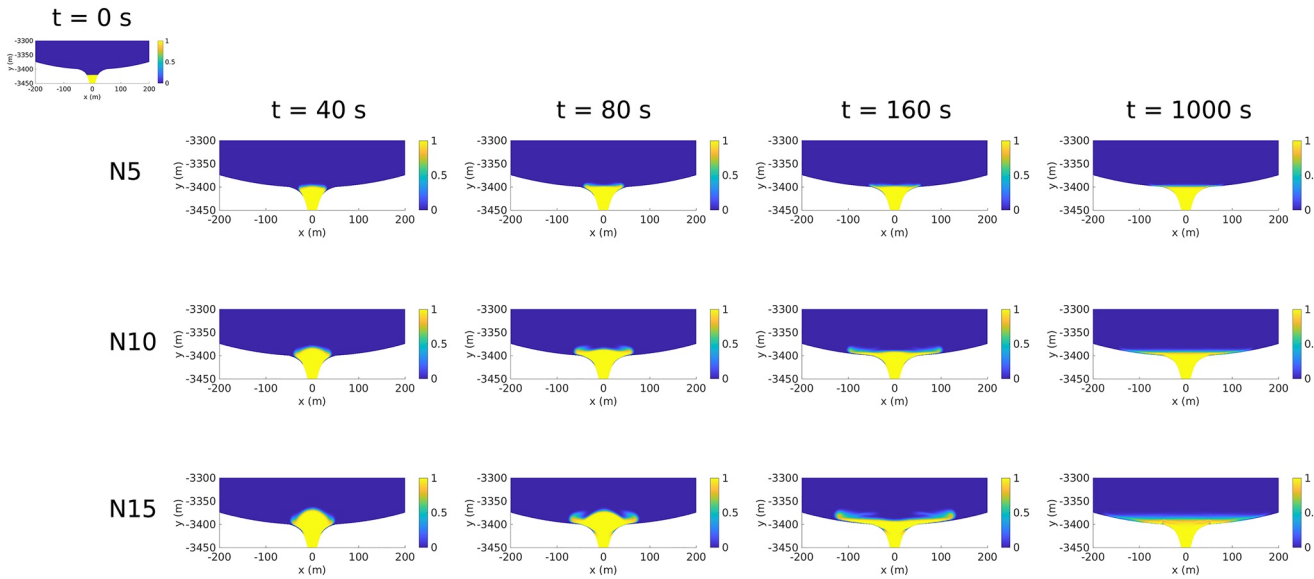

Figure 6. Computed dynamics for the three simulation cases in Table 1 with zero buoyancy. The pictures display zoom views at shallow chamber base, with the colors corresponding to composition. The $t = 0$ picture for case N5 is equal, in terms of distribution of composition, to the time zero situation for all other cases (in this figure as well as in Figure 2).

three N5, N10, and N15 simulation cases, respectively. By comparison, the P5 case with same initial overpressure as for the N5 case (5 MPa) but buoyancy also associated, injects more than 20 Mkg/m (compared to 3.2) in the first <5,000 s, and it is still injecting efficiently at that time when the simulation is terminated (Figure 3).

The initial central fountaining above the dyke and the subsequent lateral flow of dense magma along the shallow chamber bottom resembles the density currents observed in laboratory experiments and used as analogue models for the vertical layering of plutons (Irvine, 1980; Jackson, 1961). The simulated nonbuoyancy cases may reproduce the dynamics conditions for the formation of basal layers at the bottom of igneous bodies.

3.3. Overall System Dynamics

Most of the dynamics for the simulated cases concentrate in the shallow chamber + dyke system, as they are described above. Fluid motion at lower chamber level is very limited or close to null, and the observed evolution at such deep levels is nearly entirely related to pressure, the variations of which are in general important across the entire simulated domain. Pressure propagates across the entire fluid system at the local speed of sound, which depends on isentropic compressibility and is largely controlled by the local volume of gas (in turn controlled by pressure and regulated by real equation of state, contributing to system nonlinearity). For the present simulations the speed of sound varies in the range 600–1,400 m/s, depending on the specific conditions and generally increasing downwards. Accordingly, a pressure transient originating anywhere in the simulated domain propagates through the entire system in <10 s. As a consequence, although the dynamics are negligible in the deep magmatic system, pressure changes at such deep level can be important, causing variations in other important quantities such as dissolved and exsolved amounts of volatiles, gas volume and composition, and magma density and viscosity, reflecting the shallow dynamics dominated by magma intrusion and efficient convection and mixing.

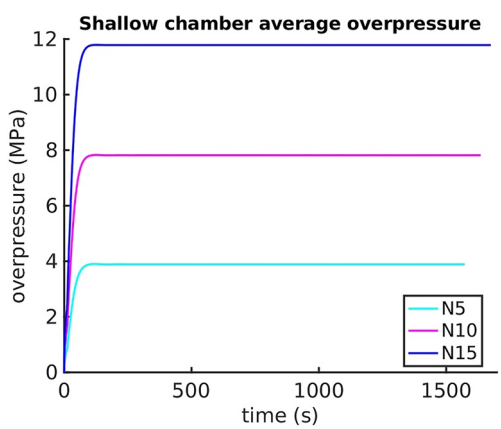

Figure 7. Evolution of the average overpressure in the shallow chamber, for the simulation cases with zero buoyancy and three different applied overpressures (cases "N" in Table 1).

Figures 8 and 9 show the evolution in the entire simulated domain of the horizontally averaged overpressure, for the simulation cases with buoyancy (Figure 8) and without buoyancy (Figure 9). The overpressure in these figures represents the change with respect to the initial conditions, which

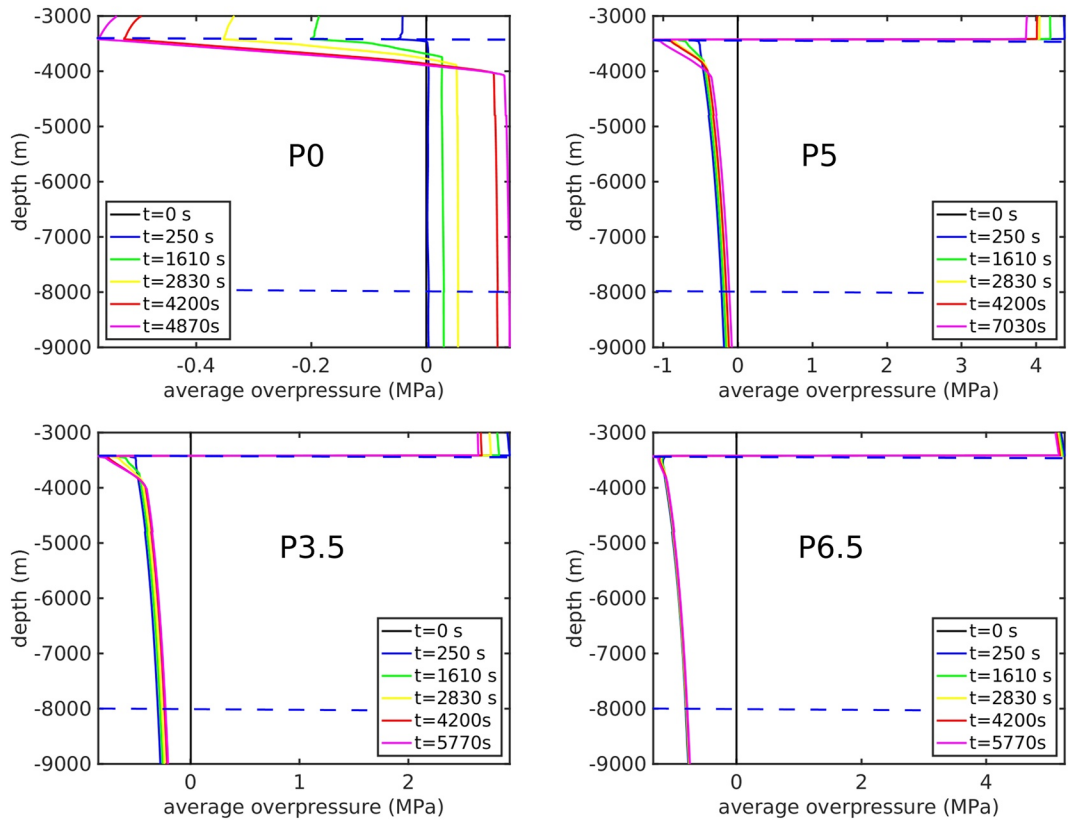

Figure 8. Pressure evolution along the entire system domain, for the four simulations with buoyancy. The lines for each time indicated in the figure represent the horizontally averaged overpressure. The thick, dashed horizontal blue lines show the extension of the three simulation subdomains represented by (from the top) the shallow chamber, the dyke, and the deep chamber (see also Figure 1). Note that the overpressure reported here refers to the conditions at time zero, therefore, the initially applied overpressure does not show up.

included an initially applied overpressure (in all cases but case P0 where such an initial overpressure is absent). The most evident feature of the pressure trends in the figures is that any variation in the upper chamber has a counterpart with opposite sign in the dyke + deep chamber domains. Accordingly, the overpressure in such deep regions is positive for the pure buoyant case P0 for which the overpressure in the shallow chamber is negative, and it is negative for all other cases. For the cases with no buoyancy (Figure 9), the overpressure is more negative for larger initial overpressure (therefore, for larger pressure increase in the chamber). For the cases with buoyancy (Figure 8) that simple relationship does not hold. Instead, the extent of negative overpressure is higher for simulation cases corresponding to larger Be/Ar (larger ratio of pressure to buoyancy force, see Table 1). The trends above suggest that buoyancy by itself, while causing a pressure decrease in the upper chamber, leads to slightly (<1 MPa) increased pressure in the deeper dyke + chamber system, likely due to compression by the dense, degassed magma sinking along the dyke. Sinking evolved magma contains less volatiles than the intruding shoshonite, thus its compressibility is smaller and smaller as depth increases and exsolved fluid tend to zero, contributing to pressure increase and introducing a small positive feedback to the upwards push of the less dense magma. Conversely, injection into the shallow chamber of initially pressurized magma, while compressing the chamber, is accompanied by release of the initial overpressure. Whenever buoyancy is a force acting on magma, sinking of dense magma accompanying convection pressurizes the deeper magmatic region, so that the overall pressure evolution at such deep levels depends on the relative importance of pressure and buoyancy forces. In all cases simulated here, with or without buoyancy or pressure forces, the distributions are such that the largest negative overpressure invariably occurs at the junction between dyke and shallow chamber. Increasing the relevance of buoyancy versus pressure leads to a region at upper dyke level characterized by large gradient of the overpressure (up to >0.1 MPa every 100 m), which is instead absent in those cases where pressure largely dominates (with the exception of a highly transient initial phase for the zero buoyancy cases, Figure 9, where the pressure gradients largely oscillate).

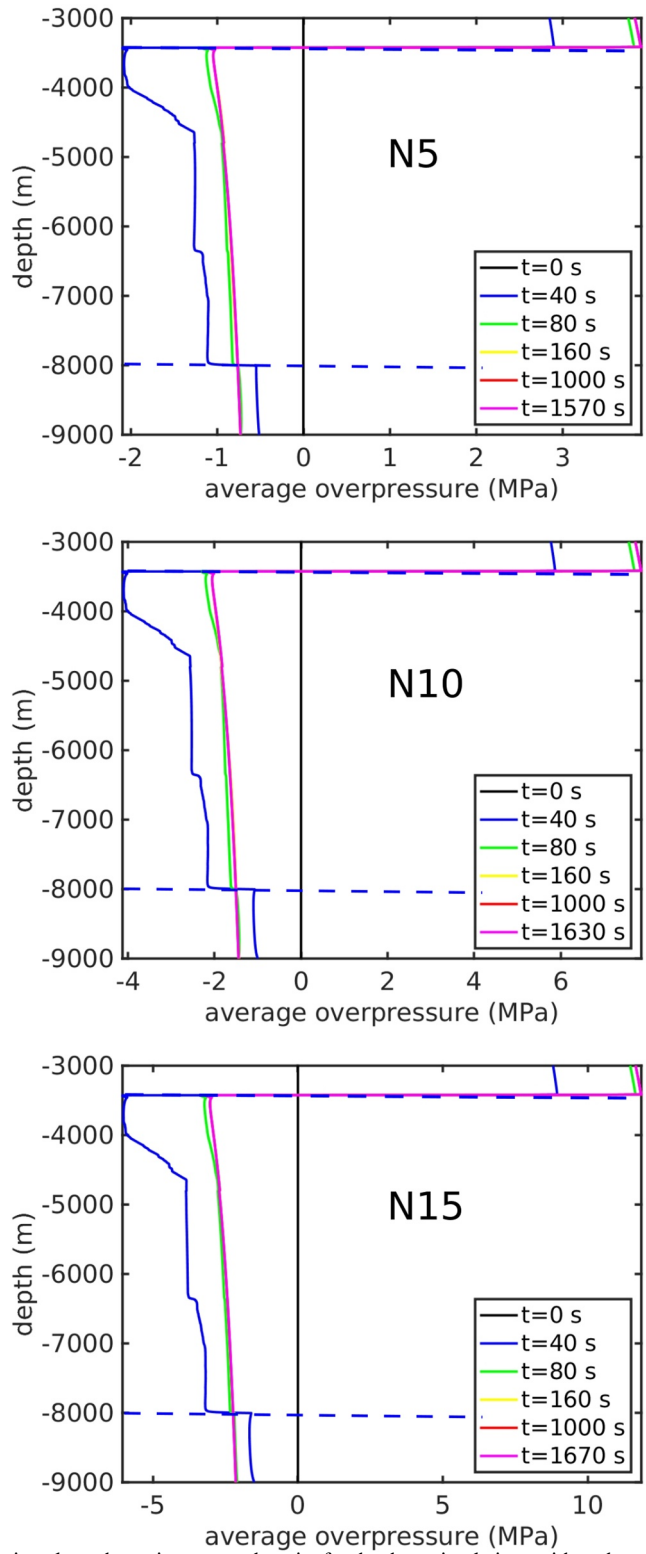

Figure 9. Pressure evolution along the entire system domain, for the three simulations without buoyancy. The lines for each time indicated in the figure represent the horizontally averaged overpressure. The thick, dashed horizontal blue lines show the extension of the three simulation subdomains represented by (from the top) the shallow chamber, the dyke, and the deep chamber (see also Figure 1). Note that the overpressure reported here refers to the conditions at time zero, therefore, the initially applied overpressure does not show up.

As it is expected, the size of the different regions plays a role in determining the magnitude of the overpressure. While compression in the shallow chamber amounts to 80%–90% of the initially applied overpressure, the parallel decompression in the deep chamber is only in the range 5%–15% of the initial overpressure. In other words, a little relative change in the density, thus in the mass, within the deep chamber, which has a 25× volume per meter with respect to the upper chamber, can accommodate for large density and mass changes occurring at shallow level.

Overall, the simulations presented here explore the dynamics of shallow magma chamber replenishment under the action of buoyancy and pressure forces. A domain much larger than the shallow chamber is included in the simulations. While each individual subdomain (shallow chamber, deep chamber, and connecting dyke) is an open system, the entire simulated domain is closed. This setup ensures consistency between the shallow evolution and the global dynamics inside a large volcanic plumbing system.

The simulation domain is necessarily a simplification of real ones, which are in fact unknown. Further complexities not included in the present analysis include the presence of crystals and mushy regions, particularly in the deep magmatic system; the existence of multiple intermediate storage regions connected through complex dyke systems hardly resembling an individual, km long, vertical one as in the present idealization; the 3D nature of the real world. The role of the assumptions made here, including three-dimensionality, domain size and shape, boundary and initial conditions for the simulations, have been discussed in Papale et al. (2017), Garg et al. (2019), and Garg and Papale (2022).

Three dimensional setups similar to those shown here yield very similar results in terms of buoyancy-driven convective dynamics: time scales of the gravitational instability are slightly different, but the overall dynamics follows similar patterns to those shown here (Garg & Papale, 2022). Domain size has an effect on the growth rate of Rayleigh-Taylor instabilities (Bellman & Pennington, 1954; Montagna et al., 2015), as well as on the times over which pressure disturbances are propagated along the whole domain. Nevertheless, the setup used in this work can represent a large number of volcanic systems characterized by relatively primitive magmas hosted in shallow, km-sized reservoirs such as Stromboli (Patanè et al., 2017), Etna (Bonaccorso & Aloisi, 2021), Kilauea (Cervelli & Miklius, 2003), Montserrat (Gunn de Rosas, 2013).

There are substantial differences between the model presented here and others that have been proposed, mostly to explain ground deformation patterns observed at volcanoes (Le Mével et al., 2016; Reverso et al., 2014; Segall, 2016) but also focusing on eruptive cycles and repose periods (Degruyter & Huber, 2014; Townsend, 2022; Townsend & Huber, 2020; Townsend et al., 2019). The model presented here includes space-time-composition dependent volatile partitioning between phases, which in turn causes the main physical properties affecting the dynamical evolution of the system, i.e., density and viscosity, to also vary as a function of space and time; and multicomponent magmatic systems. Insomuch as this description is more accurate in terms of capturing magmatic properties, solutions of our model are computationally very expensive. Moreover, our model considers a closed magmatic system, that does not exchange mass, momentum nor energy with its surroundings. This assumption is justified by the short time scales (order of a few days at most) of the processes described in this work. Pressure variations, albeit relatively small, obtained as a result of the dynamical interactions described here occur on the same short time scales. Models that reproduce observed ground deformation patterns tend to include a more simplified description of magmatic properties (density, viscosity (Le Mével et al., 2016)); they often include rock mechanics, and typically assume a continuous mass input from depth into shallow reservoirs, either explicitly or introducing pressure boundary conditions at the bottom of the modeled system (Segall, 2016). Results from these models show that pressure typically has an exponential long-term evolution toward equilibrium after an event such as an eruption, as, on average, magma flow is driven by pressure difference itself neglecting the small scale complexities included in the model presented here.

4. Conclusions

Under necessary simplifications, the present results reflect a high level of sophistication in solving the complex physics of magmatic systems, capturing a number of relevant first order aspects of the real world such as the complex relationships and feedbacks between magma compositions, multispecies volatile contents, magmatic properties, and flow variables and dynamics; and the interdependence between processes and dynamics occurring in magmatic subdomains extending over several km in depth and width. Of specific relevance for the analysis in this work are the diverse roles of buoyancy and pressure forces in driving the dynamics and determining

system evolution. In particular, buoyancy and pressure forces are found to originate very different dynamics and exert largely different controls on magma injection dynamics, leading to diverging evolutions. The present results suggest that even a slightly unstable density profile is enough to enter a regime where convection and mixing are dominant and effective; while stable density profiles translate into intrusion at chamber bottom only, with limited or no lateral flow, and limited or no mixing between the injected and resident magmas.

Thus, efficient injection, convection, and mixing dynamics typically observed in erupted products (Morgavi et al., 2017), strictly require the action of buoyancy. Convection and mixing are invariably accompanied by sinking of dense magma into the feeding dyke. In all simulated cases with buoyancy, efficient magma mixing takes place at upper dyke level, quickly causing the new magma entering the shallow chamber to lose its end-member compositional identity. That happens the faster and more effectively for larger buoyancy, irrespective of pressurization. Pressure and buoyancy forces contribute to the overall system evolution, with the former controlling the short-term dynamics, and the latter being more effective over longer times. On the short time scale a relatively fast pressure redistribution is observed, that triggers an initial high-rate injection of deep magma at shallow levels. This is followed by a much longer buoyancy-controlled phase with generally lower injection rates. The evolution of overpressure in the shallow chamber reflects such separate time scales, with an initial fast pressurization amounting to 80%–90% of the overpressure carried by the deep rising magma, followed by long-term pressure decrease of order a few tenths of MPa during the subsequent buoyancy-controlled convective phase. Space-time varying pressure trends as those observed here can have an effect on the expected ground deformation patterns recorded at volcanoes, possibly questioning some of the assumptions often used when inverting geodetic signals. The Supporting Information S1 contains comparison of the stresses acting on the reservoir walls for a Mogi model (Mogi, 1958) and for our calculations: as expected, the model predictions differ substantially from the constant-stress Mogi approximation.

Our work focuses on the Campi Flegrei caldera, but the results can be extended to other volcanic systems characterized by evidence of mingling and mixing among magmas of different compositions (Anderson, 1976; Morgavi et al., 2017). Many erupted magmas suggest a rich history of interaction and mixing between different end-members, and the literature abounds with such examples (e.g., Alves et al., 2021; Anderson, 1976; Cioni et al., 1995; Griffin et al., 2002; Ji et al., 2021; Yang et al., 2007; Zhang et al., 2021). Quite often, repetitive magma mixing events are recognized from the analysis of the erupted products, and they are usually interpreted as periodic arrivals of new magma inside a chamber (e.g., Caroff et al., 2021; Cioni et al., 1995; Civetta et al., 1991; Coppola et al., 2017; Neumann et al., 1999; Yanagi & Maeda, 1998). Based on the present results, we argue that the common condition likely to dominate much of the history of shallow magmatic bodies is that of periodic arrivals of lighter magma carrying little or no excess pressure, giving rise to efficient convection and mixing and causing limited pressure change, more negative for larger density contrast (larger Ar). Shallow level exsolution of volatiles and magma degassing which largely feeds volcanic plumes and fumaroles, either accompanied or not by cooling and crystallization of magma, provides a universal mechanism for shallow magma density increase (e.g., Girona et al., 2015). This originates buoyancy forces drawing deeper, less degassed magma toward shallow levels. Under the ubiquitous action of magma degassing at shallow level new batches of volatile-rich, light magma can be periodically brought to shallow levels, partly replacing previously degassed, dense magma sinking down, and efficiently mixing with the ascending magma. Nevertheless, care must be taken when applying our results to much more evolved magmatic compositions than those employed here (e.g., in arc settings; Ruprecht & Bachmann, 2010). In these settings, relevant physical properties, especially viscosity, can vary from what is shown in this work, resulting in very different viscosity-dominated time scales of buoyant interaction.

While buoyancy exerts a dominant control on the occurrence of magma convection and mixing, and in general controls magma injection at shallow level, there seems to be little chance for a system to evolve toward an eruption without the contribution of pressure forces: our results show that no major pressure changes are associated to buoyancy-driven mingling dynamics, which can be therefore maintained over long times.

The common process of shallow magma degassing could thus be the controlling factor originating stable conditions for periodic refilling of shallow magma chambers by buoyant magma, giving origin to repeated events of magma mixing similar to those that are observed or reconstructed at many volcanoes worldwide (Morgavi et al., 2017). These events may be related to progressive loss of exsolved fluid phases that have accumulated the top of the magmatic plumbing system (Figure 2), through fractures or pores, on time scales much longer than those simulated in this work (Aiuppa et al., 2013). Fluid loss contributes to density increase in the shallower

regions of the plumbing system, thus favoring destabilizing, buoyancy-driven mingling dynamics as magmas ascend in the crust. Similar dynamics to that described here can be seen in lava lakes: as the outer crust solidifies and becomes denser, it tends to cyclically sink and expose fresh, less dense lava from below (Witham & Llewellin, 2006).

Conversely, the occurrence of an eruption requires an important buildup of pressure over a time sufficiently short to escape any attempt by the volcanic system to re-equilibrate at the new conditions. Buoyancy-controlled magma injection dynamics by themselves are unable to achieve such pressure buildup, which instead necessarily requires some other process different from buoyancy and associated convection and mixing. Here, we simulate the case where the magma inside the dyke is overpressurized, mimicking a situation typical for dyke propagation. The simulations involving an initial overpressure may therefore be seen as starting at a time when the last diaphragm separating a rising dyke from a shallow magmatic reservoir is broken. However, our simulations do not investigate the origin of the overpressure. We can speculate on it, by invoking progressive or sudden (e.g., due to an earthquake) accumulation of tectonic stress, transients in magma production rate at depth, deep events associated with magma expansion under confined conditions, etc. Significant overpressure may also be generated directly at shallow level, e.g., due to events causing changes in the relative rates of magma exsolution and degassing (such as precipitation-induced sealing of confining rocks). In general, however, it seems that pressure buildup requires the occurrence of processes or events less obvious and universal than just shallow magma degassing originating buoyancy. Accordingly, the present results concur to provide a simple explanation for the observed long sequences of repeated shallow magma injection and mixing events which appear to represent the normal condition at most volcanoes worldwide; while the occurrence of a volcanic eruption disrupting such a dynamically stable setup requires the generation of less common conditions leading to sufficient pressure buildup somewhere in the magmatic domain.

Data Availability Statement

The `GaLeS` numerical code and the simulation setups are accessible, respectively, at https://gitlab.com/dgmaths9/gales (code repository) and at https://doi.org/10.5281/zenodo.7375639 (simulated cases).

Acknowledgments
We thank Dr. Cansu Culha and an anonymous Reviewer for their through analysis and constructive comments that helped shape the manuscript in its current form. Open Access Funding provided by Istituto Nazionale di Geofisica e Vulcanologia within the CRUI-CARE Agreement.

References

Aiuppa, A., Fischer, T. P., Plank, T., & Bani, P. (2019). CO_2 flux emissions from the Earth's most actively degassing volcanoes, 2005–2015. *Scientific Reports*, *9*(1), 5442. https://doi.org/10.1038/s41598-019-41901-y

Aiuppa, A., Tamburello, G., Di Napoli, R., Cardellini, C., Chiodini, G., Giudice, G., et al. (2013). First observations of the fumarolic gas output from a restless caldera: Implications for the current period of unrest (2005–2013) at Campi Flegrei. *Geochemistry, Geophysics, Geosystems*, *14*, 4153–4169. https://doi.org/10.1002/ggge.20261

Alves, A., de Assis Janasi, V., de Souza Pereira, G., Prado, F. A., & Munoz, P. R. (2021). Unravelling the hidden evidences of magma mixing processes via combination of in situ Sr isotopes and trace elements analyses on plagioclase crystals. *Lithos*, *404*, 106435. https://doi.org/10.1016/j.lithos.2021.106435

Anderson, A. (1976). Magma mixing: Petrological process and volcanological tool. *Journal of Volcanology and Geothermal Research*, *1*(1), 3–33. https://doi.org/10.1016/0377-0273(76)90016-0

Annen, C., Blundy, J. D., Leuthold, J., & Sparks, R. (2015). Construction and evolution of igneous bodies: Towards an integrated perspective of crustal magmatism. *Lithos*, *230*, 206–221. https://doi.org/10.1016/j.lithos.2015.05.008

Arienzo, I., Civetta, L., Heumann, A., Woerner, G., & Orsi, G. (2009). Isotopic evidence for open system processes within the Campanian Ignimbrite (Campi Flegrei—Italy) magma chamber. *Bulletin of Volcanology*, *71*(3), 285–300. https://doi.org/10.1007/s00445-008-0223-0

Arienzo, I., Heumann, A., Wörner, G., Civetta, L., & Orsi, G. (2011). Processes and timescales of magma evolution prior to the Campanian Ignimbrite eruption (Campi Flegrei, Italy). *Earth and Planetary Science Letters*, *306*(3–4), 217–228. https://doi.org/10.1016/j.epsl.2011.04.002

Arienzo, I., Moretti, R., Civetta, L., Orsi, G., & Papale, P. (2010). The feeding system of Agnano-Monte Spina eruption (Campi Flegrei, Italy): Dragging the past into present activity and future scenarios. *Chemical Geology*, *270*(1–4), 135–147. https://doi.org/10.1016/j.chemgeo.2009.11.012

Bartlett, R. W. (1969). Magma convection, temperature distribution, and differentiation. *American Journal of Science*, *267*(9), 1067–1082. https://doi.org/10.2475/ajs.267.9.1067

Bellman, R., & Pennington, R. H. (1954). Effects of surface tension and viscosity on Taylor instability. *Quarterly of Applied Mathematics*, *12*(2), 151–162. https://doi.org/10.1090/qam/63198

Bonaccorso, A., & Aloisi, M. (2021). Tracking magma storage: New perspectives from 40 years (1980–2020) of ground deformation source modeling on etna volcano. *Frontiers of Earth Science*, *9*, 638742. https://doi.org/10.3389/feart.2021.638742

Burchardt, S., Galland, O., & Németh, K. (2016). Studying volcanic plumbing systems: Multidisciplinary approaches to a multifaceted problem. In *Updates in volcanology—From volcano modelling to volcano geology* (pp. 23–53). BoD-Books on Demand.

Burgisser, A., & Degruyter, W. (2015). Magma ascent and degassing at shallow levels. In *The encyclopedia of volcanoes* (pp. 225–236). Elsevier. https://doi.org/10.1016/b978-0-12-385938-9.00011-0

Campbell, I. (1996). Fluid dynamic processes in basaltic magma chambers. *Developments in Petrology*, *15*, 45–76. https://doi.org/10.1016/S0167-2894(96)80004-2

Caroff, M., Barrat, J.-A., & Le Gall, B. (2021). Kersantites and associated intrusives from the type locality (Kersanton), Variscan Belt of Western Armorica (France). *Gondwana Research*, *98*, 46–62. https://doi.org/10.1016/j.gr.2021.06.004

Cashman, K. V., & Giordano, G. (2014). Calderas and magma reservoirs. *Journal of Volcanology and Geothermal Researc*h, *288*, 28–45. https://doi.org/10.1016/j.jvolgeores.2014.09.007

Cashman, K. V., Sparks, R., & Blundy, J. D. (2017). Vertically extensive and unstable magmatic systems: A unified view of igneous processes. *Science*, *355*(6331), eaag3055. https://doi.org/10.1126/science.aag3055

Cervelli, P. F., & Miklius, A. (2003). The shallow magmatic system of Kilauea Volcano. *U. S. Geological Survey Professional Paper*, *1676*, 149–163.

Chandrasekhar, S. (1961). *Hydrodynamic and hydromagnetic stability*. Oxford University Press.

Chiodini, G., Pappalardo, L., Aiuppa, A., & Caliro, S. (2015). The geological CO_2 degassing history of a long-lived caldera. *Geology*, *43*(9), 767–770. https://doi.org/10.1130/g36905.1

Cioni, R., Civetta, L., Marianelli, P., Metrich, N., Santacroce, R., & Sbrana, A. (1995). Compositional layering and syn-eruptive mixing of a periodically refilled shallow magma chamber: The AD 79 Plinian eruption of Vesuvius. *Journal of Petrology*, *36*(3), 739–776. https://doi.org/10.1093/petrology/36.3.739

Civetta, L., Carluccio, E., Innocenti, F., Sbrana, A., & Taddeucci, G. (1991). Magma chamber evolution under the Phlegraean Fields during the last 10 ka: Trace element and isotope data. *European Journal of Mineralogy*, *3*(2), 415–428. https://doi.org/10.1127/ejm/3/2/0415

Clark, S., Spera, F., & Yuen, D. (1987). Steady state double-diffusive convection in magma chambers heated from below. *Magmatic Processes: Physicochemical Principles*, 289–305. https://doi.org/10.1109/HICSS.2013.237

Colucci, S., & Papale, P. (2021). Deep magma transport control on the size and evolution of explosive volcanic eruptions. *Frontiers of Earth Science*, *9*, 681083. https://doi.org/10.3389/feart.2021.681083

Coppola, D., Di Muro, A., Peltier, A., Villeneuve, N., Ferrazzini, V., Favalli, M., et al. (2017). Shallow system rejuvenation and magma discharge trends at Piton de la Fournaise volcano (La Réunion Island). *Earth and Planetary Science Letters*, *463*, 13–24. https://doi.org/10.1016/j.epsl.2017.01.024

Degruyter, W., & Huber, C. (2014). A model for eruption frequency of upper crustal silicic magma chambers. *Earth and Planetary Science Letters*, *403*, 117–130. https://doi.org/10.1016/j.epsl.2014.06.047

De Siena, L., Del Pezzo, E., & Bianco, F. (2010). Seismic attenuation imaging of Campi Flegrei: Evidence of gas reservoirs, hydrothermal basins, and feeding systems. *Journal of Geophysical Research*, *115*, B09312. https://doi.org/10.1029/2009JB006938

Di Renzo, V., Arienzo, I., Civetta, L., D'Antonio, M., Tonarini, S., Di Vito, M., & Orsi, G. (2011). The magmatic feeding system of the Campi Flegrei caldera: Architecture and temporal evolution. *Chemical Geology*, *281*(3–4), 227–241. https://doi.org/10.1016/j.chemgeo.2010.12.010

Edmonds, M., Cashman, K. V., Holness, M., & Jackson, M. (2019). Architecture and dynamics of magma reservoirs. *The Royal Society Publishing*, *377*(2139), 20180298. https://doi.org/10.1098/rsta.2018.0298

Edmonds, M., Liu, E., & Cashman, K. (2022). Open-vent volcanoes fuelled by depth-integrated magma degassing. *Bulletin of Volcanology*, *84*(3), 28. https://doi.org/10.1007/s00445-021-01522-8

Garg, D., Longo, A., & Papale, P. (2018a). Computation of compressible and incompressible flows with a space–time stabilized finite element method. *Computers & Mathematics with Applications*, *75*(12), 4272–4285. https://doi.org/10.1016/j.camwa.2018.03.028

Garg, D., Longo, A., & Papale, P. (2018b). Modeling free surface flows using stabilized finite element method. *Mathematical Problems in Engineering*, *2018*, 1–9. https://doi.org/10.1155/2018/6154251

Garg, D., & Papale, P. (2022). High-performance computing of 3D magma dynamics, and comparison with 2D simulation results. *Frontiers of Earth Science*, *9*, 760773. https://doi.org/10.3389/feart.2021.760773

Garg, D., Papale, P., Colucci, S., & Longo, A. (2019). Long-lived compositional heterogeneities in magma chambers, and implications for volcanic hazard. *Scientific Reports*, *9*(1), 3321. https://doi.org/10.1038/s41598-019-40160-1

Garg, D., Papale, P., & Longo, A. (2021). A partitioned solver for compressible/incompressible fluid flow and light structure. *Computers & Mathematics with Applications*, *100*, 182–195. https://doi.org/10.1016/j.camwa.2021.09.005

Girona, T., Costa, F., & Schubert, G. (2015). Degassing during quiescence as a trigger of magma ascent and volcanic eruptions. *Scientific Reports*, *5*(1), 18212. https://doi.org/10.1038/srep18212

Gonnermann, H. M., & Manga, M. (2007). The fluid mechanics inside a volcano. *Annual Review of Fluid Mechanics*, *39*(1), 321–356. https://doi.org/10.1146/annurev.fluid.39.050905.110207

Griffin, W., Wang, X., Jackson, S., Pearson, N., O'Reilly, S. Y., Xu, X., & Zhou, X. (2002). Zircon chemistry and magma mixing, SE China: In-situ analysis of Hf isotopes, Tonglu and Pingtan igneous complexes. *Lithos*, *61*(3–4), 237–269. https://doi.org/10.1016/s0024-4937(02)00082-8

Gudmundsson, A. (2012). Magma chambers: Formation, local stresses, excess pressures, and compartments. *Journal of Volcanology and Geothermal Research*, *237*, 19–41. https://doi.org/10.1016/j.jvolgeores.2012.05.015

Gudmundsson, A. (2020). Formation and dynamics of magma chambers and reservoirs. In *Volcanotectonics: Understanding the structure, deformation and dynamics of volcanoes* (pp. 272–324). Cambridge University Press. https://doi.org/10.1017/9781139176217.007

Gunn de Rosas, C. (2013). Shallow chamber & conduit behavior of silicic magma: A thermo-and fluid-dynamic parameterization model of physical deformation as constrained by geodetic observations: Case study; Soufriere Hills Volcano, Montserrat. *AGU Fall Meeting Abstracts*, *2013*, GC51D-0996.

Irvine, T. (1980). Magmatic density currents and cumulus processes. *American Journal of Science*, *280*(Jackson Volume), 1–58.

Jackson, E. (1961). *Primary textures and mineral associations in the ultramafic zone of the Stillwater Complex, Montana*. U.S. Geol. Survey Prof. Paper.

Ji, Z., Ge, W.-C., He, Y., Bi, J.-H., Dong, Y., Yang, H., & Hao, Y.-J. (2021). Mixing of cognate magmas as a process for producing high-silica granites: Insights from Guanmenshan Complex in Liaodong Peninsula, China. *Lithos*, *406*, 106495. https://doi.org/10.1016/j.lithos.2021.106495

Judenherc, S., & Zollo, A. (2004). The Bay of Naples (southern Italy): Constraints on the volcanic structures inferred from a dense seismic survey. *Journal of Geophysical Research*, *109*, B10312. https://doi.org/10.1029/2003JB002876

Lange, R., & Carmichael, I. S. (1990). Thermodynamic properties of silicate liquids with emphasis on density, thermal expansion and compressibility. *Reviews in Mineralogy and Geochemistry*, *24*(1), 25–64.

Le Mével, H., Gregg, P. M., & Feigl, K. L. (2016). Magma injection into a long-lived reservoir to explain geodetically measured uplift: Application to the 2007–2014 unrest episode at Laguna del Maule volcanic field, Chile. *Journal of Geophysical Research: Solid Earth*, *121*, 6092–6108. https://doi.org/10.1002/2016JB013066

Longo, A., Barsanti, M., Cassioli, A., & Papale, P. (2012). A finite element Galerkin/least-squares method for computation of multicomponent compressible–incompressible flows. *Computers & Fluids*, *67*, 57–71. https://doi.org/10.1016/j.compfluid.2012.07.008

Longo, A., Papale, P., Vassalli, M., Saccorotti, G., Montagna, C., Cassioli, A., et al. (2012). Magma convection and mixing dynamics as a source of ultra-long-period oscillations. *Bulletin of Volcanology*, *74*(4), 873–880. https://doi.org/10.1007/s00445-011-0570-0

Mangiacapra, A., Moretti, R., Rutherford, M., Civetta, L., Orsi, G., & Papale, P. (2008). The deep magmatic system of the Campi Flegrei caldera (Italy). *Geophysical Research Letters*, *35*, L21304. https://doi.org/10.1029/2008GL035550
Marsh, B. D. (2015). Magma chambers. In *The encyclopedia of volcanoes* (pp. 185–201). Elsevier.
Menikoff, R., Mjolsness, R., Sharp, D., & Zemach, C. (1977). Unstable normal mode for Rayleigh-Taylor instability in viscous fluids. *The Physics of Fluids*, *20*(12), 2000–2004. https://doi.org/10.1063/1.861831
Métrich, N., Bertagnini, A., & Di Muro, A. (2010). Conditions of magma storage, degassing and ascent at Stromboli: New insights into the volcano plumbing system with inferences on the eruptive dynamics. *Journal of Petrology*, *51*(3), 603–626. https://doi.org/10.1093/petrology/egp083
Mogi, K. (1958). Relations between the eruptions of various volcanoes and the deformations of the ground surface around them. *Bulletin of the Earthquake Research*, *36*, 99–134.
Montagna, C., & Papale, P. (2018). Time scales of shallow magma chamber replenishment at Campi Flegrei caldera. (EarthArXiv). https://doi.org/10.17605/OSF.IO/KGT5P
Montagna, C., Papale, P., & Longo, A. (2015). Timescales of mingling in shallow magmatic reservoirs. *Geological Society, London, Special Publications*, *422*(1), 131–140. https://doi.org/10.1144/sp422.6
Montagna, C., Papale, P., & Longo, A. (2022). Magma chamber dynamics at the Campi Flegrei Caldera, Italy. In *Campi Flegrei* (pp. 201–217). Springer.
Morgavi, D., Arienzo, I., Montagna, C., Perugini, D., & Dingwell, D. B. (2017). Magma mixing: History and dynamics of an eruption trigger. *Volcanic Unrest*, 123–137.
Morgavi, D., Perugini, D., De Campos, C., Ertel-Ingrisch, W., & Dingwell, D. (2013a). Time evolution of chemical exchanges during mixing of rhyolitic and basaltic melts. *Contributions to Mineralogy and Petrology*, *166*(2), 615–638. https://doi.org/10.1007/s00410-013-0894-1
Morgavi, D., Perugini, D., De Campos, C. P., Ertel-Ingrisch, W., & Dingwell, D. B. (2013b). Morphochemistry of patterns produced by mixing of rhyolitic and basaltic melts. *Journal of Volcanology and Geothermal Research*, *253*, 87–96. https://doi.org/10.1016/j.jvolgeores.2012.12.007
Myers, M. L., Geist, D. J., Rowe, M. C., Harpp, K. S., Wallace, P. J., & Dufek, J. (2014). Replenishment of volatile-rich mafic magma into a degassed chamber drives mixing and eruption of Tungurahua volcano. *Bulletin of Volcanology*, *76*(11), 872. https://doi.org/10.1007/s00445-014-0872-0
Neumann, E.-R., Wulff-Pedersen, E., Simonsen, S., Pearson, N., Martí, J., & Mitjavila, J. (1999). Evidence for fractional crystallization of periodically refilled magma chambers in Tenerife, Canary Islands. *Journal of Petrology*, *40*(7), 1089–1123. https://doi.org/10.1093/petroj/40.7.1089
Oldenburg, C. M., Spera, F. J., Yuen, D. A., & Sewell, G. (1989). Dynamic mixing in magma bodies: Theory, simulations and implications. *Journal of Geophysical Research*, *94*(B7), 9215–9236. https://doi.org/10.1029/JB094iB07p09215
Orsi, G., D'Antonio, M., & Civetta, L. (2022). *Campi Flegrei: A restless caldera in a densely populated area*. Springer.
Papale, P. (2005). Determination of total H_2O and CO_2 budgets in evolving magmas from melt inclusion data. *Journal of Geophysical Research*, *110*, B03208. https://doi.org/10.1029/2004JB003033
Papale, P., Montagna, C., & Longo, A. (2017). Pressure evolution in shallow magma chambers upon buoyancy-driven replenishment. *Geochemistry, Geophysics, Geosystems*, *18*, 1214–1224. https://doi.org/10.1002/2016GC006731
Papale, P., Moretti, R., & Barbato, D. (2006). The compositional dependence of the saturation surface of $H_2O + CO_2$ fluids in silicate melts. *Chemical Geology*, *229*(1–3), 78–95. https://doi.org/10.1016/j.chemgeo.2006.01.013
Papale, P., Moretti, R., & Paonita, A. (2022). Thermodynamics of multi-component gas-melt equilibrium in magmas: Theory, models, and applications. *Reviews in Mineralogy and Geochemistry*, *87*(1), 431–556. https://doi.org/10.2138/rmg.2022.87.10
Patanè, D., Barberi, G., De Gori, P., Cocina, O., Zuccarello, L., Garcia-Yeguas, A., et al. (2017). The shallow magma chamber of Stromboli Volcano (Italy). *Geophysical Research Letters*, *44*, 6589–6596. https://doi.org/10.1002/2017GL073008
Perugini, D., De Campos, C. P., Petrelli, M., & Dingwell, D. B. (2015). Concentration variance decay during magma mixing: A volcanic chronometer. *Scientific Reports*, *5*, 14225. https://doi.org/10.1038/srep14225
Petrelli, M., Perugini, D., & Poli, G. (2011). Transition to chaos and implications for time-scales of magma hybridization during mixing processes in magma chambers. *Lithos*, *125*(1–2), 211–220. https://doi.org/10.1016/j.lithos.2011.02.007
Reverso, T., Vandemeulebrouck, J., Jouanne, F., Pinel, V., Villemin, T., Sturkell, E., & Bascou, P. (2014). A two-magma chamber model as a source of deformation at Grímsvötn Volcano, Iceland. *Journal of Geophysical Research: Solid Earth*, *119*, 4666–4683. https://doi.org/10.1002/2013JB010569
Ruprecht, P., & Bachmann, O. (2010). Pre-eruptive reheating during magma mixing at Quizapu volcano and the implications for the explosiveness of silicic arc volcanoes. *Geology*, *38*(10), 919–922. https://doi.org/10.1130/G31110.1
Segall, P. (2016). Repressurization following eruption from a magma chamber with a viscoelastic aureole. *Journal of Geophysical Research: Solid Earth*, *121*, 8501–8522. https://doi.org/10.1002/2016JB013597
Sparks, R., Annen, C., Blundy, J., Cashman, K., Rust, A., & Jackson, M. (2019). Formation and dynamics of magma reservoirs. *Philosophical Transactions of the Royal Society A*, *377*(2139), 20180019. https://doi.org/10.1098/rsta.2018.0019
Sparks, R., Blundy, J. D., Cashman, K. V., Jackson, M., Rust, A., & Wilson, C. (2022). Large silicic magma bodies and very large magnitude explosive eruptions. *Bulletin of Volcanology*, *84*(1), 8. https://doi.org/10.1007/s00445-021-01510-y
Sparks, R., & Cashman, K. V. (2017). Dynamic magma systems: Implications for forecasting volcanic activity. *Elements*, *13*(1), 35–40. https://doi.org/10.2113/gselements.13.1.35
Spera, F. J., Yuen, D. A., & Kirschvink, S. J. (1982). Thermal boundary layer convection in silicic magma chambers: Effects of temperature dependent rheology and implications for thermogravitational chemical fractionation. *Journal of Geophysical Research*, *87*(B10), 8755–8767. https://doi.org/10.1029/JB087iB10p08755
Tibaldi, A. (2015). Structure of volcano plumbing systems: A review of multi-parametric effects. *Journal of Volcanology and Geothermal Research*, *298*, 85–135. https://doi.org/10.1016/j.jvolgeores.2015.03.023
Tonarini, S., D'Antonio, M., Di Vito, M. A., Orsi, G., & Carandente, A. (2009). Geochemical and B-Sr-Nd isotopic evidence for mingling and mixing processes in the magmatic system that fed the Astroni volcano (4.1–3.8 ka) within the Campi Flegrei caldera (southern Italy). *Lithos*, *107*(3–4), 135–151. https://doi.org/10.1016/j.lithos.2008.09.012
Townsend, M. (2022). Linking surface deformation to thermal and mechanical magma chamber processes. *Earth and Planetary Science Letters*, *577*, 117272. https://doi.org/10.1016/j.epsl.2021.117272
Townsend, M., & Huber, C. (2020). A critical magma chamber size for volcanic eruptions. *Geology*, *48*(5), 431–435. https://doi.org/10.1130/g47045.1
Townsend, M., Huber, C., Degruyter, W., & Bachmann, O. (2019). Magma chamber growth during intercaldera periods: Insights from thermo-mechanical modeling with applications to Laguna del Maule, Campi Flegrei, Santorini, and Aso. *Geochemistry, Geophysics, Geosystems*, *20*, 1574–1591. https://doi.org/10.1029/2018GC008103

Wei, Z., Qin, Z., & Suckale, J. (2021). Magma mixing during conduit flow is reflected in melt-inclusion data from persistently degassing volcanoes. *Earth and Space Science Open Archive*. https://doi.org/10.1002/ESSOAR.10505766.1

Witham, F., & Llewellin, E. (2006). Stability of lava lakes. *Journal of Volcanology and Geothermal Research*, *158*(3–4), 321–332. https://doi.org/10.1016/j.jvolgeores.2006.07.004

Yanagi, T., & Maeda, S. (1998). Magma evolution observed in the Matsuura basalts in northwest Kyushu, Japan: An example of high-pressure open system fractional crystallization in a refilled magma chamber near the crust–mantle boundary. *Physics of the Earth and Planetary Interiors*, *107*(1–3), 203–219. https://doi.org/10.1016/s0031-9201(97)00134-9

Yang, J.-H., Wu, F.-Y., Wilde, S. A., Xie, L.-W., Yang, Y.-H., & Liu, X.-M. (2007). Tracing magma mixing in granite genesis: In situ U-Pb dating and Hf-isotope analysis of zircons. *Contributions to Mineralogy and Petrology*, *153*(2), 177–190. https://doi.org/10.1007/s00410-006-0139-7

Zhang, X., Guo, F., Zhang, B., Zhao, L., & Wang, G. (2021). Mixing of cogenetic magmas in the Cretaceous Zhangzhou calc-alkaline granite from southeast China recorded by in-situ apatite geochemistry. *American Mineralogist*, *106*(10), 1679–1689. https://doi.org/10.2138/am-2021-7786

Zollo, A., Maercklin, N., Vassallo, M., Dello Iacono, D., Virieux, J., & Gasparini, P. (2008). Seismic reflections reveal a massive melt layer feeding Campi Flegrei caldera. *Geophysical Research Letters*, *35*, L12306. https://doi.org/10.1029/2008GL034242